

## Article

# Microextrusion Printing of Hierarchically Structured Thick $V_2O_5$ Film with Independent from Humidity Sensing Response to Benzene

Philipp Yu. Gorobtsov <sup>\*</sup>, Artem S. Mokrushin , Tatiana L. Simonenko , Nikolay P. Simonenko, Elizaveta P. Simonenko <sup>\*</sup> and Nikolay T. Kuznetsov

Kurnakov Institute of General and Inorganic Chemistry of the Russian Academy of Sciences, 31 Leninsky pr., 119991 Moscow, Russia

<sup>\*</sup> Correspondence: phigoros@gmail.com (P.Y.G.); ep\_simonenko@mail.ru (E.P.S.)

**Abstract:** The process of  $V_2O_5$  oxide by the combination of sol-gel technique and hydrothermal treatment using heteroligand  $[VO(C_5H_7O_2)_{2-x}(C_4H_9O)_x]$  precursor was studied. Using thermal analysis, X-ray powder diffraction (XRD) and infra-red spectroscopy (IR), it was found that the resulting product was  $VO_2(B)$ , which after calcining at 300 °C (1 h), oxidized to orthorhombic  $V_2O_5$ . Scanning electron microscopy (SEM) results for  $V_2O_5$  powder showed that it consisted of nanosheets (~50 nm long and ~10 nm thick) assembled in slightly spherical hierarchic structures (diameter ~200 nm).  $VO_2$  powder dispersion was used as functional ink for microextrusion printing of oxide film. After calcining the film at 300 °C (30 min), it was found that it oxidized to  $V_2O_5$ , with SEM and atomic force microscopy (AFM) results showing that the film structure retained the hierarchic structure of the powder. Using Kelvin probe force microscopy (KPFM), the work function value for  $V_2O_5$  film in ambient conditions was calculated (4.81 eV), indicating a high amount of deficiencies in the sample.  $V_2O_5$  film exhibited selective response upon sensing benzene, with response value invariable under changing humidity. Studies of the electrical conductivity of the film revealed increased resistance due to high film porosity, with conductivity activation energy being 0.26 eV.

**Keywords:** hydrothermal synthesis;  $V_2O_5$ ;  $VO_2$ ; acetylacetonate; alkoxoacetylacetonate; work function; gas sensor; microextrusion printing; hierarchical structure; electric conductivity



**Citation:** Gorobtsov, P.Y.; Mokrushin, A.S.; Simonenko, T.L.; Simonenko, N.P.; Simonenko, E.P.; Kuznetsov, N.T. Microextrusion Printing of Hierarchically Structured Thick  $V_2O_5$  Film with Independent from Humidity Sensing Response to Benzene. *Materials* **2022**, *15*, 7837. <https://doi.org/10.3390/ma15217837>

Academic Editor: Alfonso Ibarra

Received: 13 October 2022

Accepted: 3 November 2022

Published: 7 November 2022

**Publisher's Note:** MDPI stays neutral with regard to jurisdictional claims in published maps and institutional affiliations.



**Copyright:** © 2022 by the authors. Licensee MDPI, Basel, Switzerland. This article is an open access article distributed under the terms and conditions of the Creative Commons Attribution (CC BY) license (<https://creativecommons.org/licenses/by/4.0/>).

## 1. Introduction

Nowadays, vanadium (V) oxide is one the most prospective oxide materials for a wide range of applications, owing to its structure and properties. Owing to a combination of layered structure [1] with a large amount of oxygen vacancies and vanadium reactivity in redox reactions,  $V_2O_5$  is a very promising material for various applications, such as cathode material for various ion batteries [2–6], a component of antibacterial coatings [7], photocatalysts [8], electrochromic material [9–11], charge transfer component in photovoltaics [12,13], etc. In particular,  $V_2O_5$  is a prospective receptive layer in gas sensors for the detection of  $NO_2$  [14,15],  $NH_3$  [16,17], methane [18], various volatile organic compounds (VOC)—xylene [19], trimethylamine [20], etc. Among these analytes, xylene stands out as a member of the “BTEX” family of compounds—benzene, toluene, ethylbenzene, and xylene. These substances are often used in the petrochemical industry and can often be found in its products, such as fuel, lubricants, grease, etc., as well as in other industries and products. Benzene is one of the more toxic members of the BTEX family, being a dangerous carcinogen and neurotoxin [21], as well as possessing highly flammable vapors. The presence of benzene in exhaled breath can be a tumor biomarker [22]. As a member of the BTEX species, benzene’s presence in the air is an important indicator of the overall degree of its contamination with VOCs [23]. All these factors indicate the necessity of benzene detection.

Almost each of the above-mentioned applications of  $V_2O_5$  requires its films to be prepared. There are various ways of oxide films formation, such as chemical deposition from solution (spin-coating [24–27], dip-coating [28,29]), chemical vapor deposition (CVD) [30–32], magnetron sputtering [33–35] and just brush deposition [36]. However, these techniques yield gradients in film thickness and functional properties, especially upon scaling from small to large substrate areas. These things considered, all the above-mentioned approaches possess drawbacks upon deposition of films with areas of different composition or properties, which can be necessary for the preparation of sensitive gas sensors of “electronic olfaction” unit type [37] or multicolor electrochromic displays: in order to obtain such films by using the enumerated techniques, masking a part of the surface is required, which constitutes an additional step that makes the deposition process more complicated and potentially influences the properties of already deposited oxides. Printing technologies, such as pen plotter [38,39], ink-jet [40–42], microplotter [37], and aerosol [43], allow avoiding this drawback while possessing simplicity and potential for combination with various synthesis approaches, such as sol-gel technology [37,41], hydrothermal synthesis [44,45], etc. In addition to the already mentioned printing techniques, there is a number of others, among which we dedicate special attention to microextrusion printing [46–49]. Usually, this technique is utilized in creating artificial organs in bioprinting [50], and its application in the formation of inorganic films is insufficiently studied. Microextrusion printing allows obtaining continuous lines (as well as coatings with more complex geometry) with bigger thickness per layer than in the case of ink-jet printing, for example. It is also notable for finer control over ink supply and dosage, inks can be rapidly switched without a cartridge switch, rheological requirements for inks for microextrusion printing are also much less strict, and ink dispensers are cheaper than in the case of ink-jet printing.

Dispersions of various powders can be used as inks for microextrusion printing. Thus, by varying the powder microstructure, one can influence the morphology and properties of the resulting film. Due to their highly developed surface and often due to properties of anisotropy, hierarchic oxide structures show enhanced properties compared to materials that do not exhibit such self-organization [51–55]. At the same time, hydrothermal synthesis is one of the most widespread techniques for hierarchic structure preparation [56,57]. In the case of  $V_2O_5$  hydrothermal synthesis, a narrow range of precursors is used:  $Na_3VO_4$  [58],  $(NH_4)_3VO_4$  [59], and oxalates [60]. The list of promising precursors for vanadium oxide hydrothermal synthesis can be expanded by adding hydrolytically active heteroligand complexes of  $[VO(C_5H_7O_2)_{2-x}(C_4H_9O)_x]$  species. Their hydrolysis reaction has been utilized for sol-gel preparation of  $VO_x$  [61], but, in our opinion, additional hydrothermal treatment after hydrolysis and polycondensation processes initiation for vanadium complexes widely expands our ability to control crystal structure, dispersity, and shape of resulting oxide particles.

Thus, the goal of our research was to study the process of hierarchically structured  $V_2O_5$  synthesis by combining sol-gel technology and hydrothermal treatment, as well as to study microstructure, chemosensor, and electrophysical properties of the corresponding oxide film prepared by microextrusion printing.

## 2. Materials and Methods

The general scheme of oxide powder and film preparation is given in Figure 1.

### 2.1. Oxide Powder Preparation

Hydrolytically active alkoxoacetylacetonate complex  $[VO(C_5H_7O_2)_{2-x}(C_4H_9O)_x]$  was used as a precursor. The complex was obtained following the procedure described in our [61]. Namely, n-butanol ( $C_4H_{10}O$ , 99%, Ekos-1, Moscow, Russia) solution of acetylacetonate  $[VO(C_5H_7O_2)_2]$  (98%, SigmaAldrich, St. Louis, MO, USA) underwent heat treatment for 16 h in an oil bath (bath temperature was 140 °C). The fact that vanadyl alkoxoacetylacetonate had been obtained was verified using ultra-violet (UV) and infra-red (IR) spectroscopy. Afterwards, 1 mL of  $C_2H_5OH$  (96%, Chimmed, Moscow, Russia) and distilled  $H_2O$  mixture (50% vol.  $H_2O$ ) was added to 10 mL of the precursor solution in

order to initiate hydrolysis and polycondensation processes. Then, the reaction mixture was transferred into a steel autoclave with Teflon inlay ( $V = 25$  mL), where it further underwent hydrothermal treatment at  $200$  °C for 2 h. The resulting dark green precipitate was washed with *n*-butanol several times and dried at  $60$  °C (3 h). Afterward, oxide powder was annealed in air at  $300$  °C for 30 min.

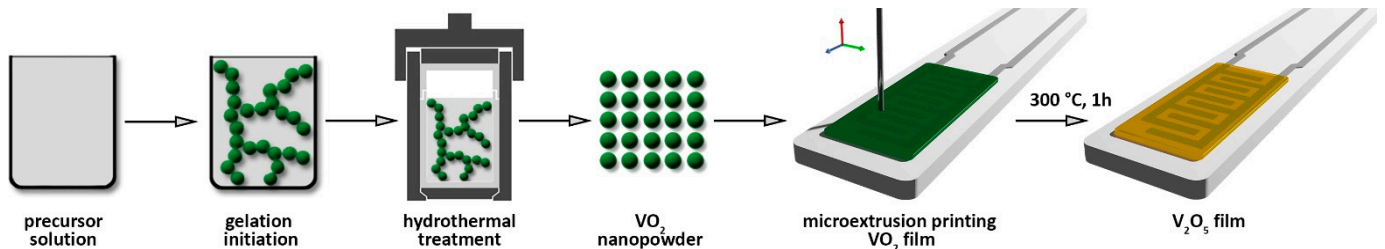


**Figure 1.** Scheme of V<sub>2</sub>O<sub>5</sub> powder and film preparation.

### 2.2. Microextrusion Printing of V<sub>2</sub>O<sub>5</sub> Film

A paste based on oxide powder (dried at  $60$  °C) and  $\alpha$ -terpineol (>97%, Acros Organics, Geel, Belgium) solution of ethylcellulose (48.0–49.5% (*w/w*) ethoxyl basis, Sigma Aldrich, St. Louis, MO, USA) was prepared in order to serve as functional ink. Microextrusion printing of oxide film on the surface of a special Pt/Al<sub>2</sub>O<sub>3</sub>/Pt chip was carried out using a 3D positioning system and pneumatic doser (pressure above ink was 1.1 atm), equipped with dispenser and G27-caliber needle (inner diameter  $210$   $\mu$ m). The speed of dispenser movement above the substrate surface was  $1$  mm/s, the time interval between impulses of paste dosing, as well as their duration, was  $0.5$  s. The chip consisted of an  $\alpha$ -Al<sub>2</sub>O<sub>3</sub> substrate ( $R_a = 100$  nm) with platinum interdigital electrodes on the face side and a platinum meander microheater on the reverse. After printing was finished, the film was dried at  $25$  °C and then calcined in air at  $300$  °C for 1 h to remove organic components and facilitate the formation of V<sub>2</sub>O<sub>5</sub> film.

### 2.3. Powder and Film Characterization

IR-spectroscopy of oxide powder after drying at  $60$  °C and annealing at  $300$  °C was recorded in the range of  $350$ – $4000$   $\text{cm}^{-1}$  using InfraLUM FT-08 IR Fourier spectrometer (Lumex, St. Petersburg, Russia), with powder suspensions in nujol mull placed between KBr lenses.

X-ray powder diffraction (XRD) spectra for oxide powder and printed film were obtained using a D8-Advance diffractometer (Bruker, Billerica, MA, USA;  $\text{CuK}\alpha 1 = 1.5418$  Å, Ni filter,  $E = 40$  keV,  $I = 40$  mA, signal accumulation time  $0.3$  s/point, resolution  $0.02^\circ$ ).

The thermal behavior of dried powder in the temperature range  $25$ – $300$  °C was studied using simultaneous TGA/DSC analyzer SDT Q600 (TA Instruments, New Castle, DE, USA), with the following regime: heating speed  $10^\circ/\text{min}$ , airflow  $250$  mL/min, with exposure at  $300$  °C for 30 min.

Oxide powder microstructure, after calcining at  $300$  °C, as well as V<sub>2</sub>O<sub>5</sub> film microstructure, was studied using scanning electron microscopy (SEM, two-beam NVision 40 workstation, Carl Zeiss, Inv., Jena, Germany).

Printed V<sub>2</sub>O<sub>5</sub> film was also studied with atomic force microscopy (AFM) using an NT-MDT Solver PRO microscope (NT-MDT, Zelenograd, Russia), with both surface morphology and local electrophysical properties of the material being characterized. In the latter case, Kelvin Probe Force Microscopy (KPFM) and Scanning Capacitance Microscopy (SCM) were utilized. All techniques were carried out in tapping mode, using ETALON HA\_HR probes (ScanSens, Bremen, Germany) with conducting W<sub>2</sub>C film (tip curvature radius  $\leq 35$  nm). During KPFM, electron work function  $\varphi_{\text{oxide}}$  was determined for oxide film. To that end, the sample surface was scanned five times using a probe with already known work function  $\varphi_{\text{tip}}$ , then for each scan the mean value of contact potential difference  $\varphi_{\text{CPD}}$  was determined. Afterwards,  $\varphi_{\text{oxide}}$  was calculated as a difference between  $\varphi_{\text{tip}}$  and  $\varphi_{\text{CPD}}$ .

Gas-sensing properties were studied using a specialized precision setup, which has been described in detail in our previous works [47,62]. Sensor responses to H<sub>2</sub>, CO, NH<sub>3</sub>, NO<sub>2</sub> and benzene (C<sub>6</sub>H<sub>6</sub>) were calculated using the following formula:

$$S = |R_g - R_{Air}| / R_{Air} \cdot 100\% \quad (1)$$

with  $R_g$  being resistance at given analyte gas concentration and  $R_{Air}$ —resistance on air.

The study of electrical conductivity for the V<sub>2</sub>O<sub>5</sub> film printed on Pt/Al<sub>2</sub>O<sub>3</sub>/Pt chip was carried out by impedance spectroscopy in the temperature range of 50–300 °C using potentiostat-galvanostat with a module for electrochemical impedance measurement (P-45X, Electrochemical Instruments, Russia, Moscow). The frequency interval for measurements was 1 MHz–1 Hz. Chip heating was carried out by applying a voltage to a platinum microheater using a power supply (QJE, PS3003, Ningbo JiuYuan Electronic, Ningbo, China), with control utilizing Testo 868 thermal imager (Testo, Titisee-Neustadt, Germany).

### 3. Results and Discussion

#### 3.1. Oxide Powder Characterization

First, the thermal behavior of the powder obtained after drying at 60 °C the precipitate formed after hydrothermal treatment was studied. It can be seen from thermograms (Figure 2a) that an endothermic effect starts at 40 °C (2 min), reaching a minimum at 71 °C (5.3 min) and ending around 101 °C (8.3 min) and accompanied by weight loss of about 7%. This can be attributed to the process of gas and organic solvent molecules desorption from the sample surface. Further heating up to 300 °C (~28 min) is accompanied by a linear decrease in weight. Several exothermic effects are observed on the differential scanning calorimetry (DSC) curve at the same time, with maxima at 173, 224, and 263 °C. These peaks can be attributed to a combination of oxidation of organic species in the sample and transformation from VO<sub>2</sub>(B) to VO<sub>2</sub>(R). After reaching 300 °C, a broadened exothermic effect occurs around 31 min, accompanied by a small (~0.15%) gain in weight. The weight gain points to the process of VO<sub>2</sub> oxidation to V<sub>2</sub>O<sub>5</sub> occurring at that moment since V<sub>2</sub>O<sub>5</sub> has more oxygen per metal ion than VO<sub>2</sub> and oxygen infiltration into the sample thus must accompany oxidation. As can be seen from the thermogravimetry analysis (TGA) curve, further holding the sample at 300 °C results in powder weight stabilization, with net weight loss being 22.6% for the full temperature range.

IR-spectroscopy results for oxide powder after drying at 60 °C and after annealing at 300 °C show (Figure 2b) that hydrothermal treatment of reactive mixture yielded vanadium dioxide, which oxidized to pentoxide after further annealing at 300 °C. This is well demonstrated by changes in IR spectra in the range of 450–1050 cm<sup>-1</sup>. Two bands related to V = O bonds vibrations can be seen for powder after drying, with maxima at 1007 and 561 cm<sup>-1</sup> [63]. After annealing at 300 °C shapes of the band around 1000 cm<sup>-1</sup> changed, a band with a maximum of 658 cm<sup>-1</sup> replaced the one with a maximum at 561 cm<sup>-1</sup>, and a new band, characteristic of bridge V-O-V bonds in V<sub>2</sub>O<sub>5</sub>, appeared at 842 cm<sup>-1</sup> [63].

X-ray powder diffraction results (Figure 2c) confirm the data from IR-spectroscopy. Reflexes in hydrothermal treatment products can all be attributed to the monoclinic VO<sub>2</sub>(B) phase (PDF card 65–7960), with small intensity and large width of the peaks hinting at the high dispersity of prepared vanadium dioxide. Full profile analysis showed that the mean coherent scattering regions (CSR) size were  $3.3 \pm 1.4$  nm, which indicates high dispersity for the product but can also be a result of its low crystallinity. Diffractogram for the powder annealed at 300 °C (30 min) is in good agreement with Inorganic Crystal Structure Database ICSD #41030 pattern and corresponds to orthorhombic V<sub>2</sub>O<sub>5</sub> (space group Pmn21). The mean CSR size, in this case, was  $20.3 \pm 5.5$  nm.

SEM data (Figure 3) shows that after annealing at 300 °C, particles of as-prepared pentoxide have the shape of nanosheets with a thickness of about 10 nm and length of 50–60 nm, assembled in hierarchical structures about 200 nm in size with well-developed surface. Particle sizes thus determined is in agreement with previously calculated mean CSR for V<sub>2</sub>O<sub>5</sub> (~20 nm).

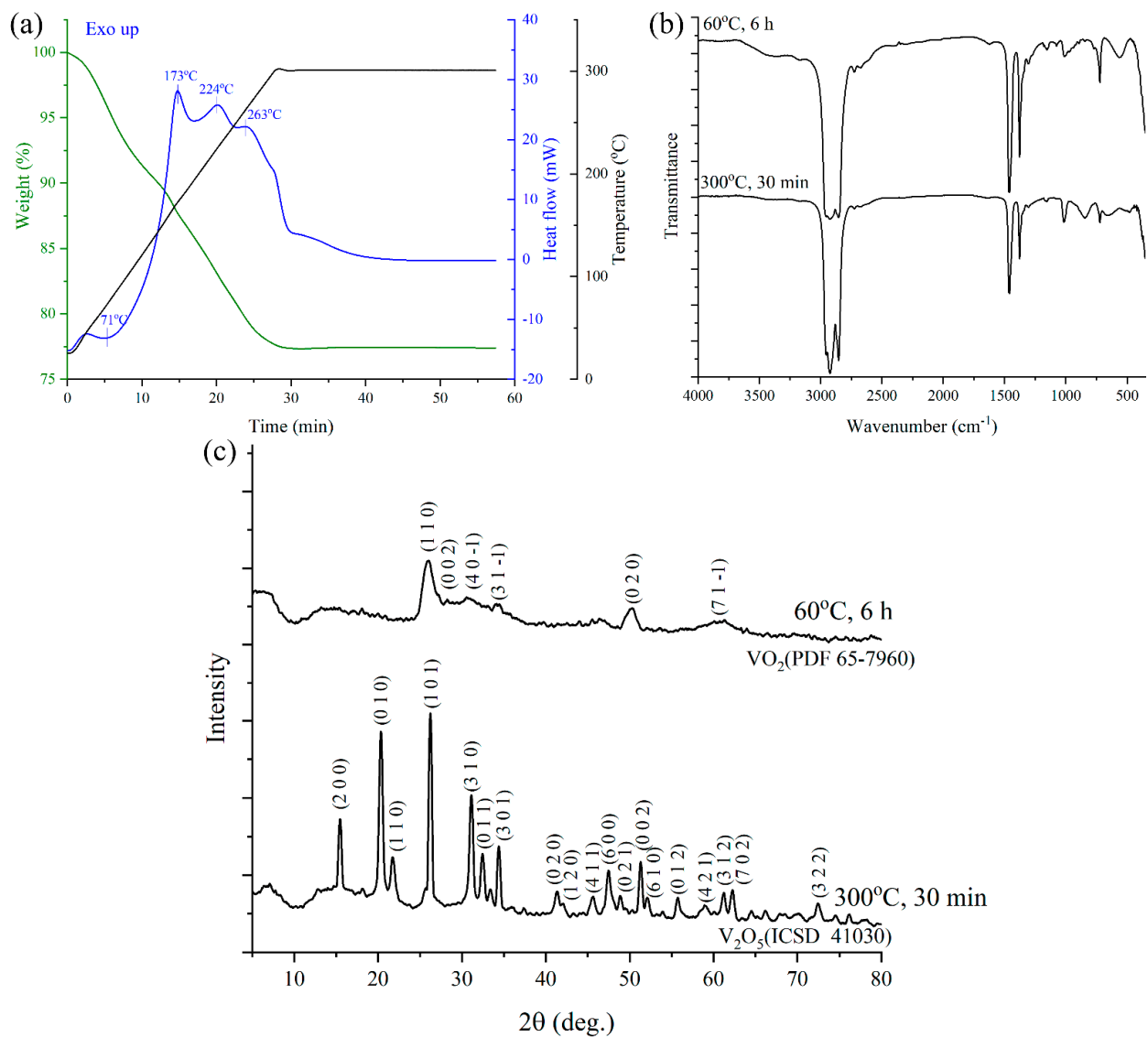


**Figure 2.** Results of simultaneous thermal analysis for oxide powder after drying: (a) IR-spectra for the powder after drying and after annealing at 300 °C; (b) Diffractograms for the powder after drying and after annealing at 300 °C (c).

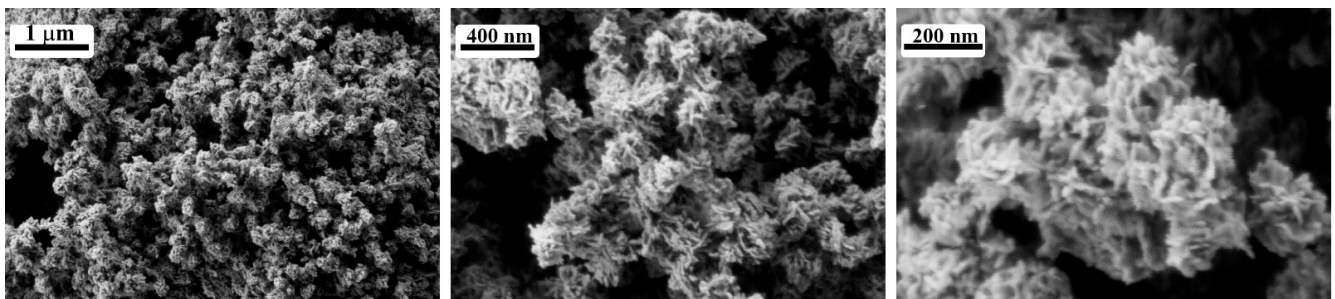


**Figure 3.** SEM results for oxide powder after annealing at 300 °C.

### 3.2. $\text{V}_2\text{O}_5$ Film Characterization

After microextrusion printing of the oxide film and annealing it at 300 °C, its phase composition was first studied. It can be seen from the recorded diffractogram (Figure 4) that the crystal structure of orthorhombic  $\text{V}_2\text{O}_5$  (space group  $\text{Pmn}21$ ; ICSD #41030) formed. Other intense peaks correspond to Pt/ $\text{Al}_2\text{O}_3$ /Pt chip materials. Thus, the steps of paste

preparation, oxide film printing, and the following annealing did not result in the appearance of any admixtures.

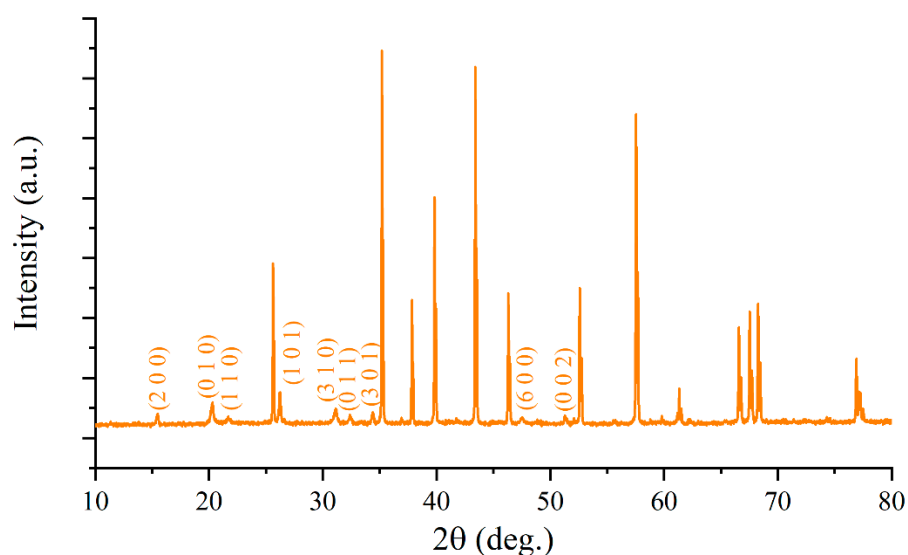


**Figure 4.** Diffractogram for  $V_2O_5$  film on Pt/ $Al_2O_3$ /Pt chip.

SEM results (Figure 5) indicate that the resulting oxide film, as well as the source powder, consists of hierarchically assembled structures based on nanosheets. The film is uniform, does not have any deficiencies such as cracks or delamination, and possesses heightened porosity. The mean size of these agglomerates is  $200 \pm 15$  nm, which correlates well with the utilized oxide powder. No admixtures with microstructure differing from the one exhibited by vanadium (V) oxide particles were found in the film.

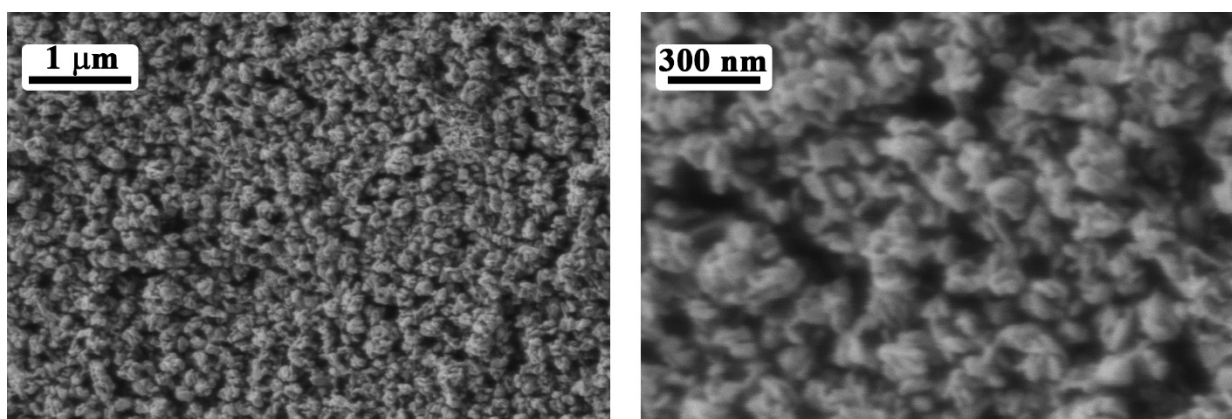


**Figure 5.** Microstructure for the printed  $V_2O_5$  film (according to SEM).

AFM results (Figure 6) confirm data obtained with SEM. Round-shaped particles with a diameter of about  $220 \pm 15$  nm are seen on topographic scans (Figure 6a,b). Their size is close to the diameter of the hierarchic oxide structures estimated using SEM ( $200 \pm 15$  nm). It can be seen from the topographic scan with an area  $100 \mu m^2$  (Figure 6a) that the film is quite uniform: even though the maximum height difference is 483 nm, the mean square roughness is just 43 nm. In addition to surface topography, the local electrophysical properties of the film were studied during AFM experiments using KPFM and SCM techniques. KPFM results (Figure 6c) show that surface potential is uniformly distributed across the studied surface (the difference between minimal and maximal values of contact potential is just 50 mV), although a small increase in its value is observed on grain boundaries, which is also evident from SCM results (Figure 6d). This implies a shift of charge carrier density and charged deficiencies into

the boundary between separate hierarchic structures. Using KPFM, the value of  $\varphi_{\text{oxide}}$  was determined for  $\text{V}_2\text{O}_5$  film, which was 4.81 eV. It is well known that  $\text{V}_2\text{O}_5$  film which has been exposed to air can have work function values in the range of 4.7–5.3 eV due to  $\text{V}^{4+}$  presence. Thus, our value of  $\varphi_{\text{oxide}}$  is in good agreement with the literature data. At the same time, a comparison of the work function for our film with those available in the literature reveals that in our case value (4.81 eV) is lower than in cases when vanadium pentoxide was prepared by vanadium (V) oxyisopropoxide  $\text{VO}(\text{C}_3\text{H}_7\text{O})_3$  (5.3 eV [64], 5.1 eV [13]), the reaction between metallic vanadium with  $\text{H}_2\text{O}_2$  (5.4 eV [65]), thermal treatment of  $\text{Na}_2\text{VO}_4$  solution (5.2 eV [66]), vanadium acid condensation (5.15–5.5 eV [67]), physical deposition from gas phase upon evaporating  $\text{V}_2\text{O}_5$  (5.1 eV [12]), but a little higher, than for vanadium pentoxide prepared by hydrothermal synthesis using sodium vanadate [58]. It is generally considered that the work function for materials based on  $\text{V}_2\text{O}_5$  is, to a large extent, determined by  $\text{V}^{4+}$  cations and oxygen vacancies content [12,68]. For example, it was shown in work [68] that a decrease in the number of oxygen vacancies and  $\text{V}^{4+}$  ions result in increased work function (from 4.73 to 5.01 eV in the referenced study). This allows assuming that in our material number of oxygen vacancies and  $\text{V}^{4+}$  ions are larger than in the case of synthesis from vanadium(V) compounds, except for hydrothermal synthesis, where it would seem a partial reduction in  $\text{V}^{5+}$  to  $\text{V}^{4+}$  occurs in the reaction mixture. It should be noted that the work function for our material differs by  $\sim 0.1$  eV from the one for vanadium oxide we earlier prepared in [61] (4.89 eV), where we utilized sol-gel technique and the same  $[\text{VO}(\text{C}_5\text{H}_7\text{O}_2)_{2-x}(\text{C}_4\text{H}_9\text{O})_x]$  precursor. Considering that the annealing regime for obtained vanadium oxide films in both studies is the same, one can assume that additional hydrothermal treatment of the reaction mixture after hydrolysis initiation yields a higher amount of deficiencies than in the case of sol-gel.

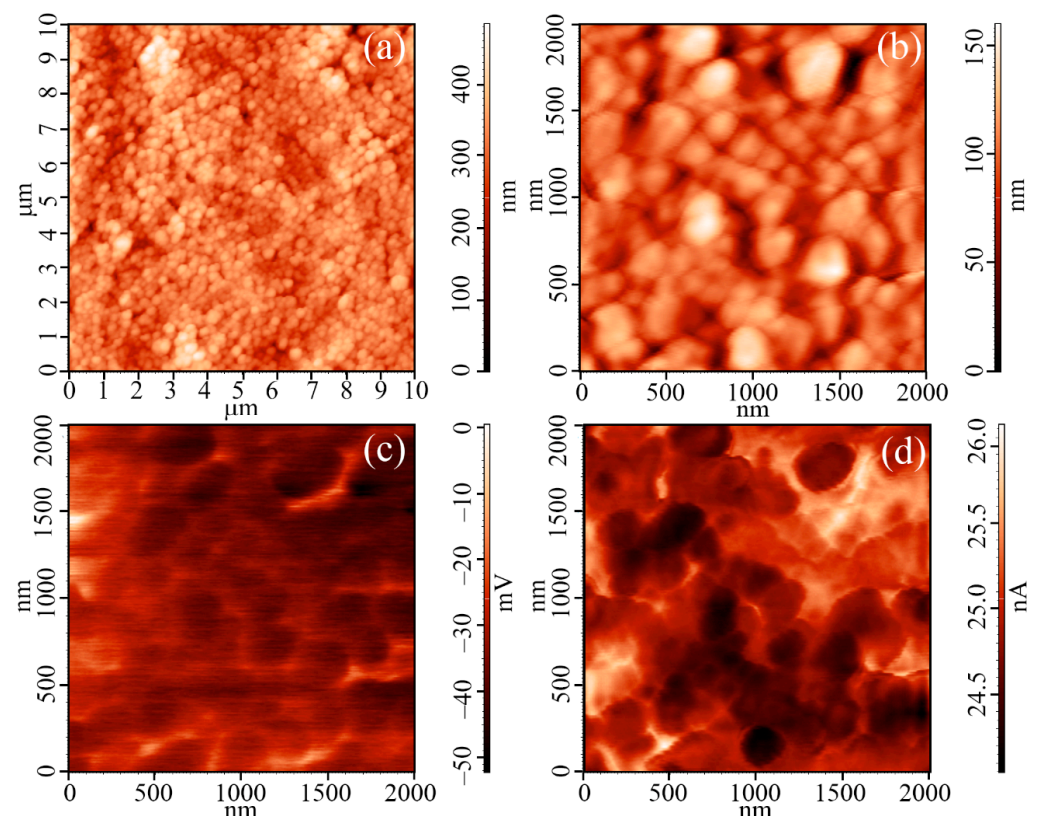


**Figure 6.** AFM results for the printed  $\text{V}_2\text{O}_5$  film: Topography (a,b), maps of potential surface distribution (c), and gradient in capacity of “probe tip-sample surface” capacitor distribution (d).

### 3.3. Sensory Properties of $\text{V}_2\text{O}_5$ Film

The prepared  $\text{V}_2\text{O}_5$  film exhibits relatively high conductivity in a wide temperature range. Out of all used analytes, the highest response was obtained for benzene (at 300 °C).

Upon studying the properties of oxide film for sensing benzene (4–100 ppm) at 300 °C (Figure 7a), it was determined that increase in concentration results in a consecutive decrease in film resistance compared to baseline and an increase in response (S) from 7 to 38%. The dependence of response (S) on benzene concentration (Figure 7b) is well described by the Freundlich equation:  $S = kCa$ , with  $k$  and  $a$  being proportional and exponential constants, which correspond to adsorption capacity and adsorption intensification, respectively [69]. In our case the equation is as follows:  $S = 7.47x^{0.37}$ , with a determination coefficient ( $R^2$ ) of 89%. This dependence is typical of chemoresistive gas sensors and is in good agreement with the literature's data [70,71]. The reproducibility of sensing responses upon detecting 20 ppm of benzene in the atmosphere with varying (0–65%) relative humidity (RH) was also studied (Figure 8a). It was established that resistance values are identical at varying humidity, which is unusual for semiconductor receptive materials in chemoresistive gas sensors. Humidity does not affect either the value of operating resistance or the response value (Figure 8b). Thus, printed  $V_2O_5$  film exhibits the same behavior at different humidity, which is important for practical application.

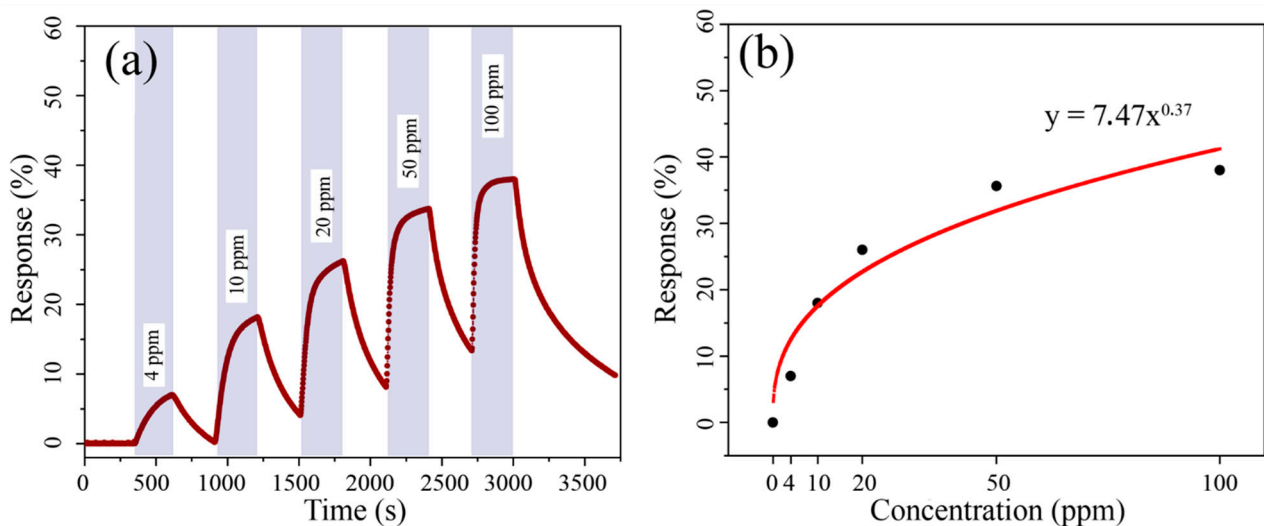


**Figure 7.** Experimental curves of changes in sensing response during detection of benzene in the concentration range of 4–100 ppm (a); Dependence of sensing response to benzene from its concentration (b).

The mechanism for detecting benzene can be described using the generally accepted views on reactions that occur between gas and semiconductor surfaces [72–75]. In ambient air at elevated temperatures, adsorption of oxygen molecules on the semiconductor surface occurs, which results in changes in material resistance due to electrons from the conduction band reducing  $O_2$  to ionic species (reaction 2). Depending on operating temperature, various ion-sorbed species can form  $O^{2-}$ ,  $O^-$ , and  $O_2^-$  [76]. At moderate operating temperatures (in particular, 300 °C),  $O^-$  particles are most likely formed. The presence of such ions on the semiconductor surface facilitates the formation of core-shell type electron structure. Inner regions of semiconductor particles become the core, while the electron depletion layer (EDL) on the surface [77], formed due to the consumption of electrons for  $O_2$  to  $O^-$  reduction becomes the shell. Interaction with benzene occurs with a redox reaction on the semiconductor surface between  $O^-$  and organic gas, with the latter undergoing oxidation (reaction 3).

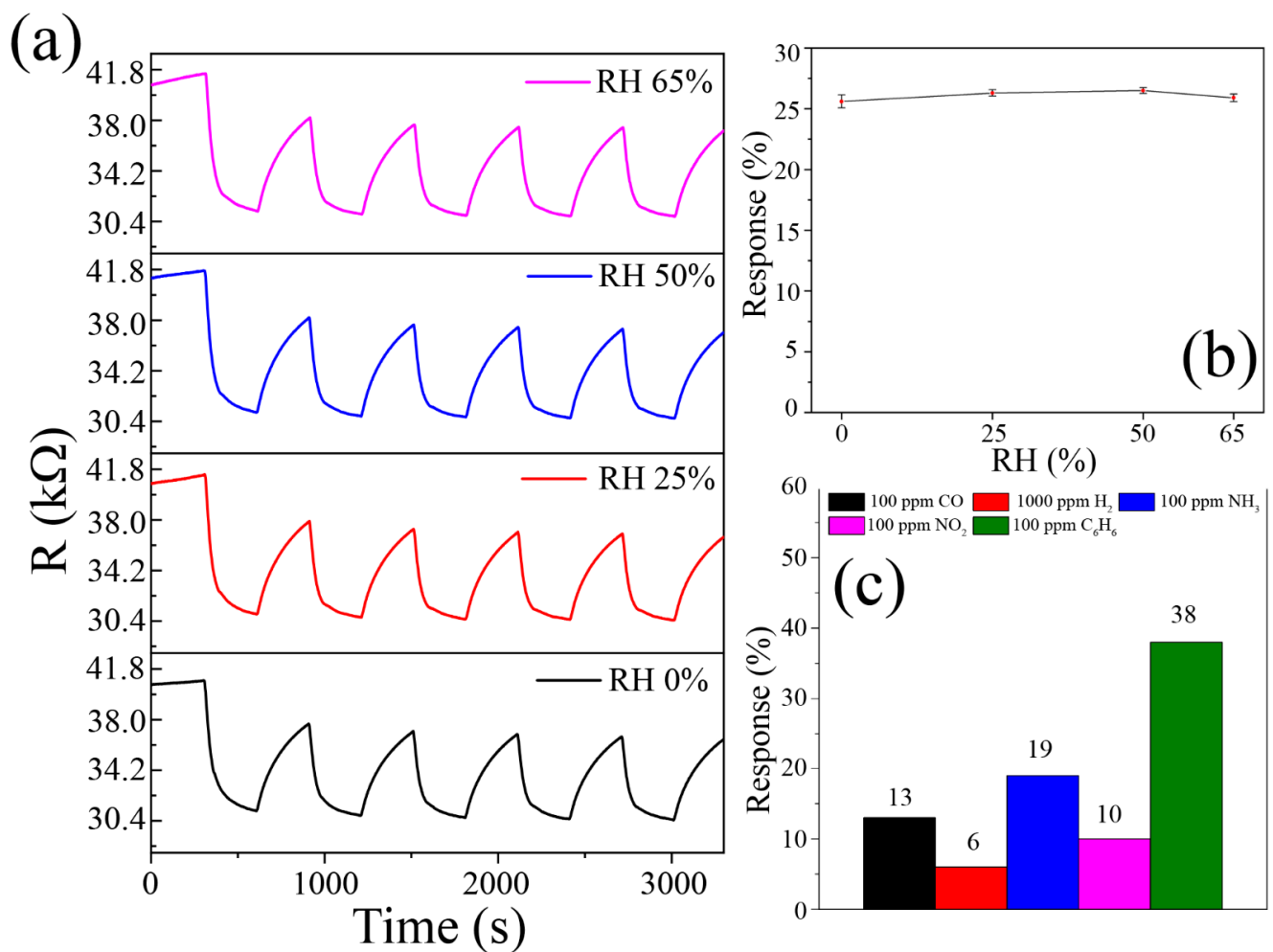
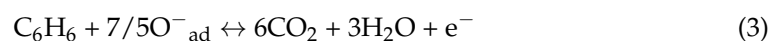
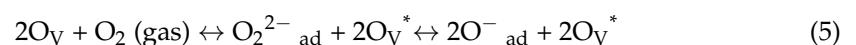


**Figure 8.** Experimental curves of resistance change upon sensing 20 ppm of benzene at varying relative humidity (a); Dependence of sensing response to 20 ppm of benzene from relative humidity (b); Selectivity diagram: sensing responses to various analyte gases at 300 °C (c).



Thus, the freed electrons enter the V<sub>2</sub>O<sub>5</sub> conduction band, resulting in resistance change (Figure 8a), which allows registering resistive response. There is a number of studies in the literature [72,73,75] where vanadium oxide was used as a component of sensors for detecting volatile organic compounds (VOCs) at moderate and high operating temperatures, which can be attributed to its catalytic activity in the oxidation of these gases due to high concentration of adsorbed oxygen species on its surface [19,78].

Another factor influencing the sensing properties is the presence and number of oxygen vacancies since they can facilitate the formation of oxygen species on the film surface, which would then react with organic gas and release additional electrons to the material conduction band, resulting in increased conductivity change and response [79]. These processes can be described by the following equations [79]:

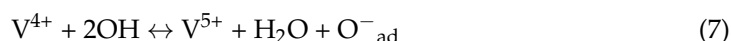


Where  $O_V^*$  is a single electropositive oxygen vacancy. As described earlier, the work function value for our material indicates a relatively large number of vacancies, which most likely positively affects sensing response and increases selectivity to benzene.

In humid air, competition between water molecules and other gases occurs for adsorption onto the oxide surface and reaction with oxygen species [21,80,81], with water forming hydroxyl groups in the course of the following reaction [81]:



Thus, it seems unlikely that oxygen vacancies significantly influence this process by themselves. There are reports, however, that show that the presence of redox-active species, such as  $Pr^{3+}/Pr^{4+}$  or  $Ce^{3+}/Ce^{4+}$ , results in practically constant sensing response under varying humidity [81,82]. In our case, a high number of  $V^{4+}$  ions (accompanying oxygen vacancies) might have the same effect by reducing hydroxyl groups back into water and turning into  $V^{5+}$ , which then is reduced back into  $V^{5+}$  by electrons from  $V_2O_5$ :



The plausibility of such a mechanism is confirmed by a number of studies, in which it was shown that hydroxyl formation is intermediate, and the final product is vanadyl bond  $V=O$  with  $V^{5+}$  [83,84]. It should be noted that in [75], where  $V_2O_5$  is used to detect xylene (another member of BTEX with a similar sensing mechanism), response changes noticeably in the range of 30–90% RH, dropping by 21% at 90% RH (and ~16% at 65% RH). That might imply that, in our case, there is a larger number of oxygen vacancies and accompanying  $V^{4+}$  ions in  $V_2O_5$ .

As a result of chemosensing measurements, a selectivity diagram for detecting 100 ppm CO,  $NH_3$ ,  $NO_2$ ,  $C_6H_6$ , and 1000 ppm  $H_2$  at 300 °C was built (Figure 8c). Selectivity to benzene is evident, with response to other gases not exceeding 19%.

Data in Table 1 allows comparing the sensing properties of our material with those reported in the literature. The comparison highlights the main advantage of our material, namely its constant response values across the studied RH range. This shows that our material is promising for practice all application.

**Table 1.** Comparison of benzene gas sensing properties of prepared  $V_2O_5$  film and several previously reported sensors.

Material	Operating Temperature, °C	$C_6H_6$ Concentration, ppm	Response S	Humidity Influence	Reference
Cr/ITO	210	166	~27%	N/A	[85]
4%Pd/TiO <sub>2</sub> /MoS <sub>2</sub> composite	Room temperature	50	65%	N/A	[86]
CoPP-TiO <sub>2</sub> <sup>1</sup>	327	9	~83%	RH↑ => S↓ <sup>2</sup>	[87]
ZnO/Au rose-like structures	206	20	~94%	N/A	[88]
0.5%Pt/ZnO spheres	250	100	~94%	N/A	[69]
ZnO/BN	300	100	~23%	S changes nonmonotonically	[21]
Co <sub>3</sub> O <sub>4</sub> hierarchical structures	160	50	~105%	N/A	[89]
Bi-SnO/rGO	150	5	~98%	RH↑ => S↓	[80]
V <sub>2</sub> O <sub>5</sub> hierarchic structures	300	100	38%	Constant S	This work

<sup>1</sup> Cobalt porphyrin-functionalized TiO<sub>2</sub>; <sup>2</sup> Humidity influence studies performed on toluene

### 3.4. Electric Conductivity of $V_2O_5$ Film

Analysis of frequency dependencies of electric conductivity (Figure 9a) for the studied film reveals two regions—the frequency-independent range (plateau from 1 to  $\sim 10^5$  Hz) and frequency-dependent range, where an increase in conductivity is observed with an increase in frequency (from 0.1 MHz and higher). The former is caused by the diffusion of mobile ions in the sample originating from applying alternating current and corresponds to the direct current conductivity  $\sigma_{dc}$ , which depends only on temperature. At a certain point, conductivity begins to increase with an increase in frequency, revealing a dispersion region that is attributed to the hopping mechanism of charge carrier transport [90]. It can be seen that an increase in temperature leads to a shifting of dispersion region to higher frequencies and an increase in alternating current conductivity  $\sigma_{ac}$ , which indicates the semiconducting nature of the material [91]. It is known that the conductivity of such materials possesses thermally activated character, i.e., higher temperatures lead to an increase in charge carrier mobility and lower semiconductor resistance [92]. The observed dependence of electrical conductivity on frequency and temperature is well described by Jonscher power law (9):

$$\sigma_{ac}(\omega, T) = \sigma_{dc}(T) + A\omega^s \quad (9)$$

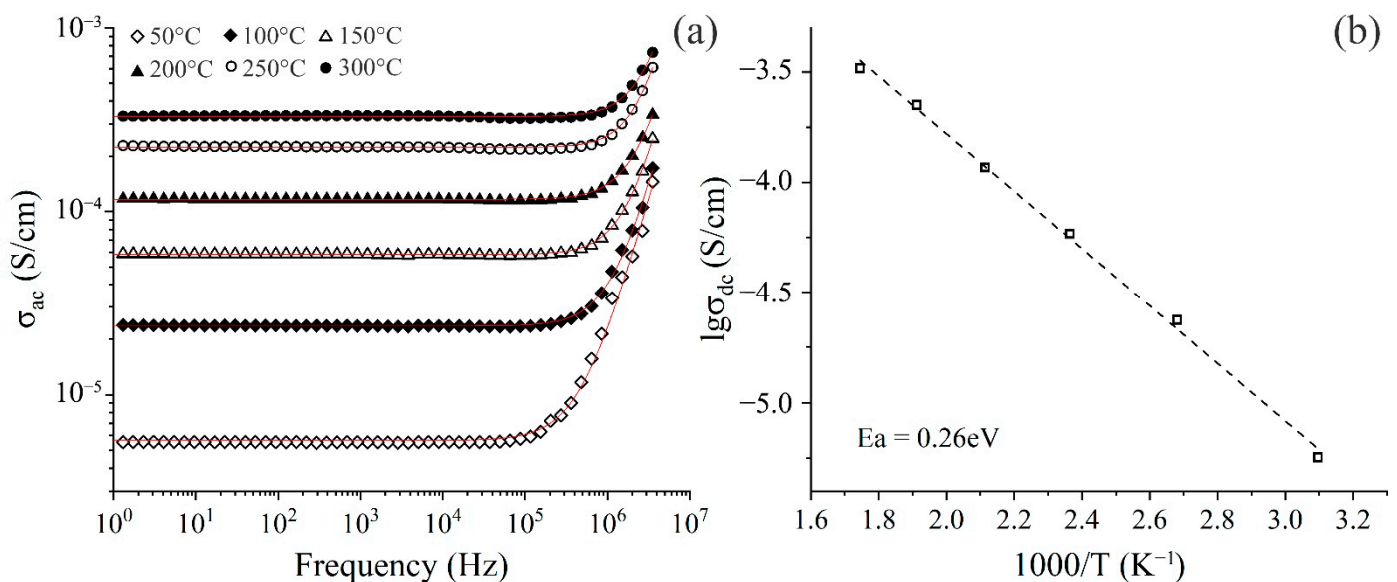


**Figure 9.** Frequency dependencies of the printed  $V_2O_5$  film conductivity at various temperatures (a); Temperature dependence of conductivity for the film (b).

With  $\sigma_{ac}$  being the conductivity value found from the real part of the total conductivity measured for alternating current,  $\sigma_{dc}$ —conductivity for direct current,  $\omega$ —angular frequency of the applied electric current,  $A$  and  $s$ —fitting coefficients determined by the nature of the studied material and dependent on temperature and frequency. In general,  $s$  has values between 0 and 1, although in some cases,  $s$  can be larger than 1.

Determining electrical conductivity values for direct current, calculated using Jonscher law, were further used for evaluating temperature dependence of conductivity (Figure 9b), as well as for calculating its activation energy by Arrhenius Equation (10):

$$\sigma_{dc} = \sigma_0 \cdot \exp(-E_a/k_B T) \quad (10)$$

with  $\sigma_0$ ,  $k_B$ ,  $E_a$  being a preexponential factor, Boltzmann constant, and activation energy for conductivity, respectively.

In the studied temperature range activation, the energy value for  $V_2O_5$  film was 0.26 eV, which is comparable to  $E_a$  values for materials of similar composition [92]. How-

ever, conductivity values are lower than those encountered in the literature for planar materials based on vanadium pentoxide [93,94]. This can be attributed to the high porosity of the printed film, which results in the decreased contact area between grains, raising material resistance.

#### 4. Conclusions

As a result of our research, the process of synthesizing hierarchically assembled  $V_2O_5$  by a combination of sol-gel technique and hydrothermal treatment using heteroligand  $[VO(C_5H_7O_2)_{2-x}(C_4H_9O)_x]$  precursor was studied. It was shown that the prepared oxide nanopowder of  $V_2O_5$  with orthorhombic crystal structure consists of hierarchic structures with a diameter of  $\sim 200$  nm, assembled from nanosheets with a length of 50–60 nm and thickness of  $\sim 10$  nm. By using functional inks based on oxide nanopowder,  $V_2O_5$  film with a similar microstructure was formed by microextrusion printing. The work function value (4.81 eV), evaluated using KPFM, allows us to assume that the chosen synthesis technique and precursor species yield an increased number of oxygen vacancies and  $V^{4+}$  ions in the material. The chemoresistive gas sensor based on the printed  $V_2O_5$  film exhibits selectivity to benzene at 300 °C. Sensing response, upon an increase in benzene concentration in the range of 4–100 ppm, rises from 7 to 38%. It should be noted that, at the same time signal does not depend on humidity. A study of the temperature dependence of printed  $V_2O_5$  film showed that activation energy value (0.26 eV) is comparable to values for similar composition materials, while electric conductivity is a little lower due to the increased porosity of the printed film.

Thus we have shown that hydrolytically active heteroligand complexes of  $[VO(C_5H_7O_2)_{2-x}(C_4H_9O)_x]$  composition is a promising precursor for the synthesis of hierarchic  $V_2O_5$  nanostructures by the combination of sol-gel technique and hydrothermal treatment, and microextrusion printing allows to efficiently form thick films based on vanadium (V) oxide with the developed surface as a receptive layer for resistive gas sensors to benzene, stable under humidity fluctuations.

**Author Contributions:** Conceptualization, N.P.S.; investigation, P.Y.G., A.S.M., T.L.S., N.P.S., E.P.S. and N.T.K.; writing—original draft preparation, P.Y.G.; writing—review and editing, N.P.S.; visualization, P.Y.G., A.S.M. and T.L.S.; supervision, E.P.S. and N.T.K. All authors have read and agreed to the published version of the manuscript.

**Funding:** The preparation of the oxide nanopowder and film in the reported study was funded by RFBR, project number 20-33-90136. The SEM and X-ray powder diffraction analyses was performed using shared experimental facilities supported by IGIC RAS state assignment.

**Institutional Review Board Statement:** Not applicable.

**Informed Consent Statement:** Not applicable.

**Data Availability Statement:** Not applicable.

**Conflicts of Interest:** The authors declare no conflict of interest.

#### References

1. Yue, Y.; Liang, H. Micro- and Nano-Structured Vanadium Pentoxide ( $V_2O_5$ ) for Electrodes of Lithium-Ion Batteries. *Adv. Energy Mater.* **2017**, *7*, 1602545. [[CrossRef](#)]
2. Tamilselvan, M.; Madhukar Sreekanth, T.V.; Yoo, K.; Kim, J. Self-Doped 2D- $V_2O_5$  Nanoflakes—A High Electrochemical Performance Cathode in Rechargeable Zinc Ion Batteries. *Ceram. Int.* **2021**, *47*, 29832–29839. [[CrossRef](#)]
3. Zhong, W.; Huang, J.; Liang, S.; Liu, J.; Li, Y.; Cai, G.; Jiang, Y.; Liu, J. New Prelithiated  $V_2O_5$  Superstructure for Lithium-Ion Batteries with Long Cycle Life and High Power. *ACS Energy Lett.* **2020**, *5*, 31–38. [[CrossRef](#)]
4. Henry, H.K.; Johnston, B.; Liau, D.; Sahadeo, E.; Lee, S.B. Dual Effect of Structure and Hydration on Magnesium-Ion Insertion into Electrodeposited  $V_2O_5$  Thin Films. *J. Electrochem. Soc.* **2020**, *167*, 110523. [[CrossRef](#)]
5. Fleischmann, S.; Leistenschneider, D.; Lemkova, V.; Krüner, B.; Zeiger, M.; Borchardt, L.; Presser, V. Tailored Mesoporous Carbon/Vanadium Pentoxide Hybrid Electrodes for High Power Pseudocapacitive Lithium and Sodium Intercalation. *Chem. Mater.* **2017**, *29*, 8653–8662. [[CrossRef](#)]
6. Diem, A.M.; Fenk, B.; Bill, J.; Burghard, Z. Binder-Free  $V_2O_5$  Cathode for High Energy Density Rechargeable Aluminum-Ion Batteries. *Nanomaterials* **2020**, *10*, 247. [[CrossRef](#)]

7. Simo, A.; Drah, M.; Sibuyi, N.R.S.; Nkosi, M.; Meyer, M.; Maaza, M. Hydrothermal Synthesis of Cobalt-Doped Vanadium Oxides: Antimicrobial Activity Study. *Ceram. Int.* **2018**, *44*, 7716–7722. [[CrossRef](#)]
8. Suresh, R.; Giribabu, K.; Manigandan, R.; Munusamy, S.; Praveen Kumar, S.; Muthamizh, S.; Stephen, A.; Narayanan, V. Doping of Co into V<sub>2</sub>O<sub>5</sub> Nanoparticles Enhances Photodegradation of Methylene Blue. *J. Alloys Compd.* **2014**, *598*, 151–160. [[CrossRef](#)]
9. Zannarini, S.; di Lupo, F.; Bedini, A.; Vankova, S.; Garino, N.; Francia, C.; Bodoardo, S. Three-Colored Electrochromic Lithiated Vanadium Oxides: The Role of Surface Superoxides in the Electro-Generation of the Red State. *J. Mater. Chem. C Mater.* **2014**, *2*, 8854–8857. [[CrossRef](#)]
10. Jin, A.; Chen, W.; Zhu, Q.; Jian, Z. Multi-Electrochromism Behavior and Electrochromic Mechanism of Electrodeposited Molybdenum Doped Vanadium Pentoxide Films. *Electrochim. Acta* **2010**, *55*, 6408–6414. [[CrossRef](#)]
11. Granqvist, C.G. Electrochromics for Smart Windows: Oxide-Based Thin Films and Devices. *Thin Solid Films* **2014**, *564*, 1–38. [[CrossRef](#)]
12. Meyer, J.; Zilberberg, K.; Riedl, T.; Kahn, A. Electronic Structure of Vanadium Pentoxide: An Efficient Hole Injector for Organic Electronic Materials. *J. Appl. Phys.* **2011**, *110*, 033710. [[CrossRef](#)]
13. Zhang, H.; Wang, S.; Sun, X.; Chen, S. Solution-Processed Vanadium Oxide as an Efficient Hole Injection Layer for Quantum-Dot Light-Emitting Diodes. *J. Mater. Chem. C Mater.* **2017**, *5*, 817–823. [[CrossRef](#)]
14. Birajdar, S.N.; Adhyapak, P. v. Palladium-Decorated Vanadium Pentoxide as NO<sub>x</sub> Gas Sensor. *Ceram. Int.* **2020**, *46*, 27381–27393. [[CrossRef](#)]
15. Mane, A.A.; Suryawanshi, M.P.; Kim, J.H.; Moholkar, A.V. Fast Response of Sprayed Vanadium Pentoxide (V<sub>2</sub>O<sub>5</sub>) Nanorods towards Nitrogen Dioxide (NO<sub>2</sub>) Gas Detection. *Appl. Surf. Sci.* **2017**, *403*, 540–550. [[CrossRef](#)]
16. Akande, A.A.; Mosuang, T.; Ouma, C.N.M.; Benecha, E.M.; Tesfamicheal, T.; Roro, K.; Machatine, A.G.J.; Mwakikunga, B.W. Ammonia Gas Sensing Characteristics of V<sub>2</sub>O<sub>5</sub> Nanostructures: A Combined Experimental and Ab Initio Density Functional Theory Approach. *J. Alloys Compd.* **2020**, *821*, 153565. [[CrossRef](#)]
17. Yin, H.; Song, C.; Wang, Z.; Shao, H.; Li, Y.; Deng, H.; Ma, Q.; Yu, K. Self-Assembled Vanadium Oxide Nanoflakes for p-Type Ammonia Sensors at Room Temperature. *Nanomaterials* **2019**, *9*, 317. [[CrossRef](#)]
18. Mounasamy, V.; Mani, G.K.; Ponnusamy, D.; Tsuchiya, K.; Reshma, P.R.; Prasad, A.K.; Madanagurusamy, S. Investigation on CH<sub>4</sub> Sensing Characteristics of Hierarchical V<sub>2</sub>O<sub>5</sub> Nanoflowers Operated at Relatively Low Temperature Using Chemiresistive Approach. *Anal. Chim. Acta* **2020**, *1106*, 148–160. [[CrossRef](#)]
19. Vijayakumar, Y.; Mani, G.K.; Ponnusamy, D.; Shankar, P.; Kulandaisamy, A.J.; Tsuchiya, K.; Rayappan, J.B.B.; Ramana Reddy, M.V. V<sub>2</sub>O<sub>5</sub> Nanofibers: Potential Contestant for High Performance Xylene Sensor. *J. Alloys Compd.* **2018**, *731*, 805–812. [[CrossRef](#)]
20. Wang, D.; Gu, K.; Zhao, Q.; Zhai, C.; Yang, T.; Lu, Q.; Zhang, J.; Zhang, M. Synthesis and Trimethylamine Sensing Properties of Spherical V<sub>2</sub>O<sub>5</sub> Hierarchical Structures. *New J. Chem.* **2018**, *42*, 14188–14193. [[CrossRef](#)]
21. Paul Choudhury, S.; Feng, Z.; Gao, C.; Ma, X.; Zhan, J.; Jia, F. BN Quantum Dots Decorated ZnO Nanoplates Sensor for Enhanced Detection of BTEX Gases. *J. Alloys Compd.* **2020**, *815*, 152376. [[CrossRef](#)]
22. Malagù, C.; Fabbri, B.; Gherardi, S.; Giberti, A.; Guidi, V.; Landini, N.; Zonta, G. Chemoresistive Gas Sensors for the Detection of Colorectal Cancer Biomarkers. *Sensors* **2014**, *14*, 18982–18992. [[CrossRef](#)] [[PubMed](#)]
23. Milazzo, M.J.; Gohlke, J.M.; Gallagher, D.L.; Scott, A.A.; Zaitchik, B.F.; Marr, L.C. Potential for City Parks to Reduce Exposure to BTEX in Air. *Environ. Sci. Process. Impacts* **2019**, *21*, 40–50. [[CrossRef](#)] [[PubMed](#)]
24. Zilberberg, K.; Trost, S.; Schmidt, H.; Riedl, T. Solution Processed Vanadium Pentoxide as Charge Extraction Layer for Organic Solar Cells. *Adv. Energy Mater.* **2011**, *1*, 377–381. [[CrossRef](#)]
25. Hajzeri, M.; Šurca Vuk, A.; Slemenik Perše, L.; Čolović, M.; Herbig, B.; Posset, U.; Kržmanc, M.; Orel, B. Sol-Gel Vanadium Oxide Thin Films for a Flexible Electronically Conductive Polymeric Substrate. *Sol. Energy Mater. Sol. Cells* **2012**, *99*, 62–72. [[CrossRef](#)]
26. Fradi, K.; Bouich, A.; Slimi, B.; Chtourou, R. Towards Improving the Optoelectronics Properties of MAPb<sub>3(1-x)</sub>B<sub>3x</sub>/ZnO Heterojunction by Bromine Doping. *Optik* **2022**, *249*, 168283. [[CrossRef](#)]
27. Sahana, M.B.; Sudakar, C.; Thapa, C.; Lawes, G.; Naik, V.M.; Baird, R.J.; Auner, G.W.; Naik, R.; Padmanabhan, K.R. Electrochemical Properties of V<sub>2</sub>O<sub>5</sub> Thin Films Deposited by Spin Coating. *Mater. Sci. Eng. B* **2007**, *143*, 42–50. [[CrossRef](#)]
28. Gökdemir, F.P.; Özdemir, O.; Kutlu, K. Comparison of Structural and Electrochemical Properties of V<sub>2</sub>O<sub>5</sub> Thin Films Prepared by Organic/Inorganic Precursors. *Electrochim. Acta* **2014**, *121*, 240–244. [[CrossRef](#)]
29. Glynn, C.; Creedon, D.; Geaney, H.; O’Connell, J.; Holmes, J.D.; O’Dwyer, C. Optimizing Vanadium Pentoxide Thin Films and Multilayers from Dip-Coated Nanofluid Precursors. *ACS Appl. Mater. Interfaces* **2014**, *6*, 2031–2038. [[CrossRef](#)]
30. Vernardou, D.; Paterakis, P.; Drosos, H.; Spanakis, E.; Povey, I.M.; Pemble, M.E.; Koudoumas, E.; Katsarakis, N. A Study of the Electrochemical Performance of Vanadium Oxide Thin Films Grown by Atmospheric Pressure Chemical Vapour Deposition. *Sol. Energy Mater. Sol. Cells* **2011**, *95*, 2842–2847. [[CrossRef](#)]
31. Drosos, C.; Jia, C.; Mathew, S.; Palgrave, R.G.; Moss, B.; Kafizas, A.; Vernardou, D. Aerosol-Assisted Chemical Vapor Deposition of V<sub>2</sub>O<sub>5</sub> Cathodes with High Rate Capabilities for Magnesium-Ion Batteries. *J. Power Sources* **2018**, *384*, 355–359. [[CrossRef](#)]
32. Nandakumar, N.K.; Seebauer, E.G. Low Temperature Chemical Vapor Deposition of Nanocrystalline V<sub>2</sub>O<sub>5</sub> Thin Films. *Thin Solid Films* **2011**, *519*, 3663–3668. [[CrossRef](#)]
33. Raj, P.D.; Gupta, S.; Sridharan, M. Influence of the Crystalline Nature of Growing Surface on the Properties of Vanadium Pentoxide Thin Films. *Ceram. Int.* **2017**, *43*, 9401–9407. [[CrossRef](#)]

34. Zou, C.W.; Yan, X.D.; Han, J.; Chen, R.Q.; Gao, W. Microstructures and Optical Properties of  $\beta$ -V<sub>2</sub>O<sub>5</sub> Nanorods Prepared by Magnetron Sputtering. *J. Phys. D Appl. Phys.* **2009**, *42*, 145402. [[CrossRef](#)]
35. Quinzeni, I.; Ferrari, S.; Quartarone, E.; Mustarelli, P. Structural, Morphological and Electrochemical Properties of Nanocrystalline V<sub>2</sub>O<sub>5</sub> Thin Films Deposited by Means of Radiofrequency Magnetron Sputtering. *J. Power Sources* **2011**, *196*, 10228–10233. [[CrossRef](#)]
36. Cho, S.P.; Yeo, J.S.; Kim, D.Y.; Na, S.I.; Kim, S.S. Brush Painted V<sub>2</sub>O<sub>5</sub> Hole Transport Layer for Efficient and Air-Stable Polymer Solar Cells. *Sol. Energy Mater. Sol. Cells* **2015**, *132*, 196–203. [[CrossRef](#)]
37. Fedorov, F.S.; Simonenko, N.P.; Trouillet, V.; Volkov, I.A.; Plugin, I.A.; Rupasov, D.P.; Mokrushin, A.S.; Nagornov, I.A.; Simonenko, T.L.; Vlasov, I.S.; et al. Microplotter-Printed On-Chip Combinatorial Library of Ink-Derived Multiple Metal Oxides as an “Electronic Olfaction” Unit. *ACS Appl. Mater. Interfaces* **2020**, *12*, 56135–56150. [[CrossRef](#)]
38. Simonenko, T.L.; Simonenko, N.P.; Gorobtsov, P.Y.; Mokrushin, A.S.; Solovey, V.R.; Pozharnitskaya, V.M.; Simonenko, E.P.; Glumov, O.V.; Melnikova, N.A.; Lizunova, A.A.; et al. Pen Plotter Printing of Co<sub>3</sub>O<sub>4</sub> Thin Films: Features of the Microstructure, Optical, Electrophysical and Gas-Sensing Properties. *J. Alloys Compd.* **2020**, *832*, 154957. [[CrossRef](#)]
39. Simonenko, T.L.; Simonenko, N.P.; Gorobtsov, P.Y.; Pozharnitskaya, V.M.; Simonenko, E.P.; Glumov, O.V.; Melnikova, N.A.; Sevastyanov, V.G.; Kuznetsov, N.T. Pen Plotter Printing of MnO<sub>x</sub> Thin Films Using Manganese Alkoxyacetylacetonate. *Russ. J. Inorg. Chem.* **2021**, *66*, 1416–1424. [[CrossRef](#)]
40. Jeong, J.-A.; Lee, J.; Kim, H.; Kim, H.-K.; Na, S.-I. Ink-Jet Printed Transparent Electrode Using Nano-Size Indium Tin Oxide Particles for Organic Photovoltaics. *Sol. Energy Mater. Sol. Cells* **2010**, *94*, 1840–1844. [[CrossRef](#)]
41. Costa, C.; Pinheiro, C.; Henriques, I.; Laia, C.A.T. Electrochromic Properties of Inkjet Printed Vanadium Oxide Gel on Flexible Polyethylene Terephthalate/Indium Tin Oxide Electrodes. *ACS Appl. Mater. Interfaces* **2012**, *4*, 5266–5275. [[CrossRef](#)] [[PubMed](#)]
42. Costa, C.; Pinheiro, C.; Henriques, I.; Laia, C.A.T. Inkjet Printing of Sol-Gel Synthesized Hydrated Tungsten Oxide Nanoparticles for Flexible Electrochromic Devices. *ACS Appl. Mater. Interfaces* **2012**, *4*, 1330–1340. [[CrossRef](#)] [[PubMed](#)]
43. Fedorov, F.S.; Simonenko, N.P.; Arsenov, P.V.; Zaytsev, V.; Simonenko, T.L.; Goikhman, B.V.; Volkov, I.A.; Simonenko, E.P.; Nasibulin, A.G. Study of Programmed Co-Precipitation of Aluminum Doped Zinc Oxide for High Precision Design of Gas Analytical Units. *Appl. Surf. Sci.* **2022**, *606*, 154717. [[CrossRef](#)]
44. Černá, M.; Veselý, M.; Dzik, P.; Guillard, C.; Puzenat, E.; Lepičová, M. Fabrication, Characterization and Photocatalytic Activity of TiO<sub>2</sub> layers Prepared by Inkjet Printing of Stabilized Nanocrystalline Suspensions. *Appl. Catal. B Environ.* **2013**, *138*, 84–94. [[CrossRef](#)]
45. Simonenko, N.P.; Fisenko, N.A.; Fedorov, F.S.; Simonenko, T.L.; Mokrushin, A.S.; Simonenko, E.P.; Korotcenkov, G.; Sysoev, V.V.; Sevastyanov, V.G.; Kuznetsov, N.T. Printing Technologies as an Emerging Approach in Gas Sensors: Survey of Literature. *Sensors* **2022**, *22*, 3473. [[CrossRef](#)]
46. Seo, H.; Iwai, H.; Kishimoto, M.; Ding, C.; Saito, M.; Yoshida, H. Microextrusion Printing for Increasing Electrode–Electrolyte Interface in Anode-Supported Solid Oxide Fuel Cells. *J. Power Sources* **2020**, *450*, 227682. [[CrossRef](#)]
47. Mokrushin, A.S.; Simonenko, T.L.; Simonenko, N.P.; Gorobtsov, P.; Bocharova, V.A.; Kozodaev, M.G.; Markeev, A.M.; Lizunova, A.A.; Volkov, I.A.; Simonenko, E.P.; et al. Microextrusion Printing of Gas-Sensitive Planar Anisotropic NiO Nanostructures and Their Surface Modification in an H<sub>2</sub>S Atmosphere. *Appl. Surf. Sci.* **2022**, *578*, 151984. [[CrossRef](#)]
48. Simonenko, N.P.; Kadyrov, N.S.H.; Simonenko, T.L.; Simonenko, E.P.; Sevastyanov, V.G.; Kuznetsov, N.T. Preparation of ZnS Nanopowders and Their Use in the Additive Production of Thick-Film Structures. *Russ. J. Inorg. Chem.* **2021**, *66*, 1283–1288. [[CrossRef](#)]
49. Simonenko, T.L.; Simonenko, N.P.; Gorobtsov, P.Y.; Klyuev, A.L.; Grafov, O.Yu.; Ivanova, T.M.; Simonenko, E.P.; Sevastyanov, V.G.; Kuznetsov, N.T. Hydrothermally Synthesized Hierarchical Ce<sub>1</sub>-XSm<sub>x</sub>O<sub>2- $\delta$</sub>  Oxides for Additive Manufacturing of Planar Solid Electrolytes. *Ceram. Int.* **2022**, *48*, 22442–22451. [[CrossRef](#)]
50. Noor, N.; Shapira, A.; Edri, R.; Gal, I.; Wertheim, L.; Dvir, T. 3D Printing of Personalized Thick and Perfusable Cardiac Patches and Hearts. *Adv. Sci.* **2019**, *6*, 1900344. [[CrossRef](#)]
51. Simonenko, T.L.; Bocharova, V.A.; Gorobtsov, P.Y.; Simonenko, N.P.; Simonenko, E.P.; Sevastyanov, V.G.; Kuznetsov, N.T. Features of Hydrothermal Growth of Hierarchical Co<sub>3</sub>O<sub>4</sub> Coatings on Al<sub>2</sub>O<sub>3</sub> Substrates. *Russ. J. Inorg. Chem.* **2020**, *65*, 1304–1311. [[CrossRef](#)]
52. Simonenko, T.L.; Bocharova, V.A.; Gorobtsov, P.Y.; Simonenko, N.P.; Muradova, A.G.; Simonenko, E.P.; Sevastyanov, V.G.; Kuznetsov, N.T. Formation of Hierarchical NiO Coatings on the Surface of Al<sub>2</sub>O<sub>3</sub> Substrates under Hydrothermal Conditions. *Russ. J. Inorg. Chem.* **2020**, *65*, 1292–1297. [[CrossRef](#)]
53. Martin-Martinez, F.J.; Jin, K.; López Barreiro, D.; Buehler, M.J. The Rise of Hierarchical Nanostructured Materials from Renewable Sources: Learning from Nature. *ACS Nano* **2018**, *12*, 7425–7433. [[CrossRef](#)] [[PubMed](#)]
54. Zheng, M.; Tang, H.; Li, L.; Hu, Q.; Zhang, L.; Xue, H.; Pang, H. Hierarchically Nanostructured Transition Metal Oxides for Lithium-Ion Batteries. *Adv. Sci.* **2018**, *5*, 1700592. [[CrossRef](#)]
55. Wang, H.; Rogach, A.L. Hierarchical SnO<sub>2</sub> Nanostructures: Recent Advances in Design, Synthesis, and Applications. *Chem. Mater.* **2014**, *26*, 123–133. [[CrossRef](#)]
56. Sui, L.; Yu, T.; Zhao, D.; Cheng, X.; Zhang, X.; Wang, P.; Xu, Y.; Gao, S.; Zhao, H.; Gao, Y.; et al. In Situ Deposited Hierarchical CuO/NiO Nanowall Arrays Film Sensor with Enhanced Gas Sensing Performance to H<sub>2</sub>S. *J. Hazard. Mater.* **2020**, *385*, 121570. [[CrossRef](#)]

57. Zhang, H.; Chen, W.; Li, Y.; Song, Z.; Zeng, W.; Tang, S.; Wang, S.; Zhou, D. Hierarchical Heterostructures of Nanosheet-Assembled NiO-Modified ZnO Microflowers for High Performance Acetylene Detection. *Ceram. Int.* **2020**, *46*, 3574–3581. [[CrossRef](#)]
58. Reddy, B.N.; Mukkabla, R.; Deepa, M.; Ghosal, P. Dual Purpose Poly(3,4-Ethylenedioxyppyrrrole)/Vanadium Pentoxide Nanobelt Hybrids in Photoelectrochromic Cells and Supercapacitors. *RSC Adv.* **2015**, *5*, 31422–31433. [[CrossRef](#)]
59. Dou, Y.; Liang, X.; Gao, G.; Wu, G. Template-Free Synthesis of Porous V<sub>2</sub>O<sub>5</sub> Yolk-Shell Microspheres as Cathode Materials for Lithium Ion Batteries. *J. Alloys Compd.* **2018**, *735*, 109–116. [[CrossRef](#)]
60. Margoni, M.M.; Mathuri, S.; Ramamurthi, K.; Babu, R.R.; Ganesh, V.; Sethuraman, K. Hydrothermally Grown Nano and Microstructured V<sub>2</sub>O<sub>5</sub> Thin Films for Electrochromic Application. *Appl. Surf. Sci.* **2018**, *449*, 193–202. [[CrossRef](#)]
61. Gorobtsov, P.Y.; Fisenko, N.A.; Solovey, V.R.; Simonenko, N.P.; Simonenko, E.P.; Volkov, I.A.; Sevastyanov, V.G.; Kuznetsov, N.T. Microstructure and Local Electrophysical Properties of Sol-Gel Derived (In<sub>2</sub>O<sub>3</sub>–10%SnO<sub>2</sub>)/V<sub>2</sub>O<sub>5</sub> Films. *Colloids Interface Sci. Commun.* **2021**, *43*, 100452. [[CrossRef](#)]
62. Mokrushin, A.S.; Simonenko, T.L.; Simonenko, N.P.; Gorobtsov, P.Y.; Kadyrov, N.C.; Simonenko, E.P.; Sevastyanov, V.G.; Kuznetsov, N.T. Chemoresistive Gas-Sensing Properties of Highly Dispersed Nb<sub>2</sub>O<sub>5</sub> Obtained by Programmable Precipitation. *J. Alloys Compd.* **2021**, *868*, 159090. [[CrossRef](#)]
63. Botto, I.L.; Vassallo, M.B.; Baran, E.J.; Minelli, G. IR Spectra of VO<sub>2</sub> and V<sub>2</sub>O<sub>3</sub>. *Mater. Chem. Phys.* **1997**, *50*, 267–270. [[CrossRef](#)]
64. Zilberberg, K.; Trost, S.; Meyer, J.; Kahn, A.; Behrendt, A.; Lützenkirchen-Hecht, D.; Frahm, R.; Riedl, T. Inverted Organic Solar Cells with Sol-Gel Processed High Work-Function Vanadium Oxide Hole-Extraction Layers. *Adv. Funct. Mater.* **2011**, *21*, 4776–4783. [[CrossRef](#)]
65. Peng, H.; Sun, W.; Li, Y.; Ye, S.; Rao, H.; Yan, W.; Zhou, H.; Bian, Z.; Huang, C. Solution Processed Inorganic V<sub>2</sub>O<sub>x</sub> as Interfacial Function Materials for Inverted Planar-Heterojunction Perovskite Solar Cells with Enhanced Efficiency. *Nano Res.* **2016**, *9*, 2960–2971. [[CrossRef](#)]
66. Navyashree, G.R.; Hareesh, K.; Sunitha, D.V.; Nagabhushana, H.; Nagaraju, G. Photocatalytic Degradation Performance of Nd<sup>3+</sup> Doped V<sub>2</sub>O<sub>5</sub> Nanostructures. *Mater. Res. Express* **2018**, *5*, 095007. [[CrossRef](#)]
67. Terán-Escobar, G.; Pampel, J.; Caicedo, J.M.; Lira-Cantú, M. Low-Temperature, Solution-Processed, Layered V<sub>2</sub>O<sub>5</sub> Hydrate as the Hole-Transport Layer for Stable Organic Solar Cells. *Energy Environ. Sci.* **2013**, *6*, 3088–3098. [[CrossRef](#)]
68. Choi, S.G.; Seok, H.J.; Rhee, S.; Hahm, D.; Bae, W.K.; Kim, H.K. Magnetron-Sputtered Amorphous V<sub>2</sub>O<sub>5</sub> Hole Injection Layer for High Performance Quantum Dot Light-Emitting Diode. *J. Alloys Compd.* **2021**, *878*, 160303. [[CrossRef](#)]
69. Mokrushin, A.S.; Nagornov, I.A.; Simonenko, T.L.; Simonenko, N.P.; Gorobtsov, P.; Khamova, T.V.; Kopitsa, G.P.; Evzrezov, A.N.; Simonenko, E.P.; Sevastyanov, V.G.; et al. Chemoresistive Gas-Sensitive ZnO/Pt Nanocomposites Films Applied by Microplotter Printing with Increased Sensitivity to Benzene and Hydrogen. *Mater. Sci. Eng. B* **2021**, *271*, 115233. [[CrossRef](#)]
70. Ambardekar, V.; Bandyopadhyay, P.P.; Majumder, S.B. Understanding on the Ethanol Sensing Mechanism of Atmospheric Plasma Sprayed 25 wt. % WO<sub>3</sub>-75 wt. % SnO<sub>2</sub> Coating. *Sens. Actuators B Chem.* **2019**, *290*, 414–425. [[CrossRef](#)]
71. McConnell, C.; Kanakaraj, S.N.; Dugre, J.; Malik, R.; Zhang, G.; Haase, M.R.; Hsieh, Y.Y.; Fang, Y.; Mast, D.; Shanov, V. Hydrogen Sensors Based on Flexible Carbon Nanotube-Palladium Composite Sheets Integrated with Ripstop Fabric. *ACS Omega* **2020**, *5*, 487–497. [[CrossRef](#)] [[PubMed](#)]
72. Ezhilan, M.; JBB, A.J.; Balaguru Rayappan, J.B. Influence of PVA Templates on the Synthesis of Interconnected and Long-Winded Electrospun V<sub>2</sub>O<sub>5</sub> Nanowires—Acetone Sensor. *Mater. Res. Bull.* **2021**, *139*, 111276. [[CrossRef](#)]
73. Tadeo, I.J.; Parasuraman, R.; Umarji, A.M. Highly Sensitive and Selective Ultrasonically Nebulized V<sub>2</sub>O<sub>5</sub> Thin Films towards Ethanol and NO<sub>2</sub> Gas Detection. *Sens. Actuators B Chem.* **2021**, *337*, 129811. [[CrossRef](#)]
74. Hien, V.X.; Thang, T.M.; Dong, V.T.; Nhat, D.D.; Nghi, N.T.; Phuoc, L.H.; Khoa, C.T.; Vuong, D.D.; Chien, N.D. Synthesis of VO<sub>2</sub> Thin Films from Vanadium Powder and Determination of Room-Temperature NH<sub>3</sub> Sensing Properties. *J. Mater. Sci. Mater. Electron.* **2021**, *32*, 13803–13812. [[CrossRef](#)]
75. Cao, P.J.; Gui, X.G.; Pawar, D.; Han, S.; Xu, W.Y.; Fang, M.; Liu, X.K.; Zeng, Y.X.; Liu, W.J.; Zhu, D.L.; et al. Highly Ordered Mesoporous V<sub>2</sub>O<sub>5</sub> Nanospheres Utilized Chemiresistive Sensors for Selective Detection of Xylene. *Mater. Sci. Eng. B* **2021**, *265*, 115031. [[CrossRef](#)]
76. Kim, H.J.; Lee, J.H.; Hyo-Joong, K.; Jong-Heun, L. Highly Sensitive and Selective Gas Sensors Using P-Type Oxide Semiconductors: Overview. *Sens. Actuators B Chem.* **2014**, *192*, 607–627. [[CrossRef](#)]
77. Jeong, S.Y.; Kim, J.S.; Lee, J.H. Rational Design of Semiconductor-Based Chemiresistors and Their Libraries for Next-Generation Artificial Olfaction. *Adv. Mater.* **2020**, *32*, 2002075. [[CrossRef](#)]
78. Nagaraju, P.; Vijayakumar, Y.; Reddy, M.V.R.; Deshpande, U.P. Effect of Vanadium Pentoxide Concentration in ZnO/V<sub>2</sub>O<sub>5</sub> Nanostructured Composite Thin Films for Toluene Detection. *RSC Adv.* **2019**, *9*, 16515–16524. [[CrossRef](#)]
79. Wang, Y.; Gao, R.; Zhao, H.; Li, J.; Zhang, R.; Wang, Y.; Zhou, Y. Oxygen Vacancy-rich ZnO Nanorods-based MEMS Sensors for Swift Trace Ethanol Recognition. *J. Am. Ceram. Soc.* **2022**, 1–12. [[CrossRef](#)]
80. Guo, W.; Zhou, Q.; Zhang, J.; Fu, M.; Radacsi, N.; Li, Y. Hydrothermal Synthesis of Bi-Doped SnO<sub>2</sub>/RGO Nanocomposites and the Enhanced Gas Sensing Performance to Benzene. *Sens. Actuators B Chem.* **2019**, *299*, 126959. [[CrossRef](#)]
81. Kim, J.S.; Na, C.W.; Kwak, C.H.; Li, H.Y.; Yoon, J.W.; Kim, J.H.; Jeong, S.Y.; Lee, J.H. Humidity-Independent Gas Sensors Using Pr-Doped In<sub>2</sub>O<sub>3</sub> Macroporous Spheres: Role of Cyclic Pr<sup>3+</sup>/Pr<sup>4+</sup> Redox Reactions in Suppression of Water-Poisoning Effect. *ACS Appl. Mater. Interfaces* **2019**, *11*, 25322–25329. [[CrossRef](#)] [[PubMed](#)]

82. Yoon, J.W.; Kim, J.S.; Kim, T.H.; Hong, Y.J.; Kang, Y.C.; Lee, J.H. A New Strategy for Humidity Independent Oxide Chemiresistors: Dynamic Self-Refreshing of In<sub>2</sub>O<sub>3</sub> Sensing Surface Assisted by Layer-by-Layer Coated CeO<sub>2</sub> Nanoclusters. *Small* **2016**, *12*, 4229–4240. [[CrossRef](#)] [[PubMed](#)]
83. Avdeev, V.I.; Tapilin, V.M. Water Effect on the Electronic Structure of Active Sites of Supported Vanadium Oxide Catalyst VO<sub>x</sub>/TiO<sub>2</sub>(001). *J. Phys. Chem. C* **2010**, *114*, 3609–3613. [[CrossRef](#)]
84. Goodacre, D.; Blum, M.; Buechner, C.; Hoek, H.; Gericke, S.M.; Jovic, V.; Franklin, J.B.; Kittiwatanakul, S.; Söhnle, T.; Bluhm, H.; et al. Water Adsorption on Vanadium Oxide Thin Films in Ambient Relative Humidity. *J. Chem. Phys.* **2020**, *152*, 044715. [[CrossRef](#)] [[PubMed](#)]
85. Vaishnav, V.S.; Patel, S.G.; Panchal, J.N. Development of ITO Thin Film Sensor for Detection of Benzene. *Sens. Actuators B Chem.* **2015**, *206*, 381–388. [[CrossRef](#)]
86. Zhang, D.; Jiang, C.; Zhou, X. Fabrication of Pd-Decorated TiO<sub>2</sub>/MoS<sub>2</sub> Ternary Nanocomposite for Enhanced Benzene Gas Sensing Performance at Room Temperature. *Talanta* **2018**, *182*, 324–332. [[CrossRef](#)]
87. Kang, Y.; Kim, K.; Cho, B.; Kwak, Y.; Kim, J. Highly Sensitive Detection of Benzene, Toluene, and Xylene Based on CoPP-Functionalized TiO<sub>2</sub> Nanoparticles with Low Power Consumption. *ACS Sens.* **2020**, *5*, 754–763. [[CrossRef](#)]
88. Shen, Z.; Zhang, X.; Ma, X.; Mi, R.; Chen, Y.; Ruan, S. The Significant Improvement for BTX (Benzene, Toluene and Xylene) Sensing Performance Based on Au-Decorated Hierarchical ZnO Porous Rose-like Architectures. *Sens. Actuators B Chem.* **2018**, *262*, 86–94. [[CrossRef](#)]
89. Cao, J.; Wang, S.; Li, J.; Xing, Y.; Zhao, X.; Li, D. Porous Nanosheets Assembled Co<sub>3</sub>O<sub>4</sub> Hierarchical Architectures for Enhanced BTX (Benzene, Toluene and Xylene) Gas Detection. *Sens. Actuators B Chem.* **2020**, *315*, 128120. [[CrossRef](#)]
90. Jonscher, A.K. The “universal” Dielectric Response. *Nature* **1977**, *267*, 673–679. [[CrossRef](#)]
91. Khan, S.; Singh, K. Effect of MgO on Structural, Thermal and Conducting Properties of V<sub>2-x</sub>Mg<sub>x</sub>O<sub>5-δ</sub> (X = 0.05–0.30) Systems. *Ceram. Int.* **2019**, *45*, 695–701. [[CrossRef](#)]
92. Khan, S.; Singh, K. Influence of Al<sub>3</sub><sup>+</sup> Doping for V<sub>5</sub><sup>+</sup> on the Structural, Optical, Thermal and Electrical Properties of V<sub>2-x</sub>Al<sub>x</sub>O<sub>5-δ</sub> (X = 0–0.20) Ceramics. *Ceram. Int.* **2021**, *47*, 10724–10732. [[CrossRef](#)]
93. Kang, M.; Jung, J.; Lee, S.Y.; Ryu, J.W.; Kim, S.W. Conductivity, Carrier Density, Mobility, Seebeck Coefficient, and Power Factor in V<sub>2</sub>O<sub>5</sub>. *Thermochim. Acta* **2014**, *576*, 71–74. [[CrossRef](#)]
94. Schneider, K.; Dziubaniuk, M.; Wyrwa, J. Impedance Spectroscopy of Vanadium Pentoxide Thin Films. *J. Electron. Mater.* **2019**, *48*, 4085–4091. [[CrossRef](#)]